

Deciphering coastal shoreline dynamics in the Mesopotamian Delta: Integrating 48-year Landsat time series (1976–2024), decision matrix analysis and future projections for Ras al Bisha, Iraqi coast

Bassim Mohammed Hashim^{1,*}, Nadheer A. Fazaa², Maitham A. Sultan¹, Basim A. Hussain¹, Esam Abd Alraheem¹

Abstract

The Iraqi coast, particularly the Ras al Bisha region at the mouth of the Shatt al-Arab, is among the most sensitive regions to coastal changes due to the complex interplay between natural factors and human activities. This study analyzed spatial and temporal changes in the Ras al Bisha coastline over a 48-year period (1976, 1990, 2000, 2013, and 2024) using Landsat and the Digital Shoreline Analysis System (DSAS). Statistical indicators (NSM, SCE, LRR, and EPR) were calculated, spatial changes analyzed, and a decision matrix developed to assess the intensity of erosion-accretion, with projections for 2035 and 2045. Quantitative results revealed that coastal erosion dominated 75% of the sections, particularly in the central and western areas, with maximum erosion rates of -16.7 m/year (average: -5.56 m/year). Net accretion reached 1.84 km² in the eastern region, while erosion reached 1.44 km² in the western and central regions (1976–2024). Results revealed a clear temporal alternation between erosion-dominated periods (1976–1990 and 2000–2013) and accretion dominated periods (1990–2000 and 2013–2024). LULC classification achieved 92.5% accuracy ($Kappa = 0.91$). Coastal Vulnerability Index (CVI) analysis identified zones F, B, and D as high risk areas ($CVI = 12.91$ – 14.43) requiring urgent coastal management interventions. Future projections to 2045 indicated a baseline shoreline advance of $+32.55$ m, with continued eastward expansion of Ras al Bisha. The study's novelty lies in integrating advanced DSAS analysis with comprehensive spatial analysis frameworks, decision matrix, and future projections, providing a dynamic and holistic assessment of coastal dynamics at Ras al Bisha. Unbalanced spatial distribution of erosion and accretion reflects complex interactions between natural factors (Shamal winds, ocean currents) and human activities (new Faw port, dredging). This study recommends adopting of an integrated coastal management system for Iraq, incorporating continuous remote sensing monitoring, advanced predictive modeling, and targeted engineering and environmental interventions to mitigate erosion risks and safeguard coastal infrastructure.

Keywords

Iraqi coastline; Ras al Bisha; Landsat images; DSAS; Decision matrix; CVI

¹Scientific Research Commission, Baghdad, Iraq

²Ministry of Environment, Baghdad, Iraq

*Correspondence: bassim_hashim@src.edu.iq (B.M. Hashim)

Received: 13 November 2025; revised: 31 March 2026; accepted: 4 May 2026

1. Introduction

The Arabian Gulf (also known as the Persian Gulf) is one of the world's most strategically important regions, hosting vast oil and gas reserves and extensive coastal and maritime infrastructure projects (Mussa et al., 2024). Spanning 990 km in length, with a maximum width of 370 km and mean depth of 36 m, this semi-enclosed body of water

represents a critical ecosystem and economic zone (Lafta, 2021). Assessment of erosion hazards, identification of potentially dangerous coastal locations, and provision of evidence based references for disaster prevention plans all depend fundamentally on shoreline change analysis (Ozturk and Sesli, 2015; Santos et al., 2021). Understanding these processes is crucial for coastal management. Coastal degradation – manifested through ecosystem loss, land subsidence, and elevated threats to infrastructure and hu-

man populations – results from complex interactions between natural and anthropogenic processes (Fernández-Hernández et al., 2023). Shoreline dynamics, driven by erosion and accretion, are influenced by multiple factors including fluvial discharge, wave action, tidal processes, and human interventions such as breakwaters, marinas, and dredging operations. Understanding these dynamics requires integrated quantitative and spatial analysis approaches (El-Masry, 2022).

Iraq's marine waters, encompassing the Shatt al-Arab River and associated lagoons, represent the most estuarine region of the northern Arabian Gulf and serve as the primary freshwater source to this basin (Lafta, 2021, 2023). Erosion and accretion in Ras al Bisha results from both natural and anthropogenic drivers. Natural factors include the dramatic decline of the Shatt al-Arab from approximately $1191 \text{ m}^3/\text{s}$ in the late 1970s to roughly $50 \text{ m}^3/\text{s}$ by 2018, reducing sediment supply by 4–9 million tons/year (Khalifa, 2019; Al-Asadi and Muttashar, 2022). Additional natural stressors include sea-level rise at 3–5 mm/year, and land subsidence at 1–2 cm/year (Muttashar et al., 2024). Anthropogenic factors include the new Faw port diverting currents and upstream dams on the Euphrates and Tigris rivers.

Remote sensing and Geographic Information Systems (GIS) have become indispensable tools for coastal management and planning (Yasir et al., 2024). Satellite platforms such as Landsat have enabled continuous monitoring of coastline position changes over multiple decades, facilitating both risk assessment and adaptive management strategies (Vos et al., 2019; El Kafrawy and Ahmed, 2020; Palomar-Vázquez et al., 2023). The Digital Shoreline Analysis System (DSAS) a GIS based tool employing multidimensional statistical approaches provides high-accuracy quantification of spatial variations in shoreline dynamics over time, with applicability across diverse coastal environments globally. Unlike automated extraction algorithms (which offer low accuracy in complex coastal areas) or machine learning methods (which require large training datasets and lack statistical transparency), DSAS provides integrated statistical indicators with comprehensive error and uncertainty handling (Saad et al., 2021; Darwish and Smith, 2023). This methodological advantage makes DSAS particularly suitable for the complex coastal environment of Ras al Bisha.

Recent DSAS-based studies have documented significant shoreline changes across the Arabian Gulf and globally. Al-Fartusi et al. (2023) analyzed the entire Iraqi coastline over five decades (1973–2021) using Landsat imagery and DSAS, confirming widespread erosion with maximum rates in Ras al Bisha near new Faw port, attributed to altered sedimentation patterns and declining Shatt al-Arab discharge. Muttashar et al. (2024) used multitemporal bathymetric maps and geotechnical sediment characteristics to evaluate the Iraqi coastline in Khor Abdullah from 1966 to

2019, finding that erosion is the dominant threat with an average shoreline erosion of -3.48 m/year in Ras al Bisha and the northern Faw district. However, these studies lack three crucial elements: (1) future forecasts required by integrated coastal management; (2) comprehensive classification of erosion severity grades applicable to decision-making; and (3) systematic linkage between natural factors and human-made structures. Similarly, studies of the North Sinai coast, Egypt (1989–2016) reported maximum coastal erosion of -8.17 m/year in El Tinah Bay (Nassar et al. 2019). While analysis of the Vishakhapatnam district coast, India, revealed heterogeneous shoreline dynamics with high erosion occupying 5.8 km, moderate accretion along 30.5 km, and high accretion over 17.8 km (Baig et al., 2020). Recent assessments of the Oman coastline (2000–2022) demonstrated that human activities exert greater influence on coastal change than natural factors, with artificial structures dominating natural shoreline patterns (Colak, 2024). While these studies provide valuable insights, they reveal important gaps that the current research addresses.

At the global scale, emerging research emphasizes the integration of satellite-based vulnerability indicators for coastal erosion management. Queiroz et al. (2022) characterized global satellite-based indicators for coastal vulnerability assessment, highlighting remote sensing's critical importance in coastal decision-making. Mishra et al. (2023) conducted quantitative assessment of shoreline changes along the Odisha coast, integrating geospatial tools and statistical techniques. Paul et al. (2024b) elucidated overwash vulnerability and shoreline dynamics in Sagar Island (2000–2020). These studies collectively underscore the necessity for comprehensive, multi-decadal assessments integrating quantitative shoreline analysis with spatial decision frameworks and future projections.

Recent studies have applied DSAS-based shoreline analysis in lake environments using Google Earth Engine (GEE). For instance, Gümüş et al. (2022) used DSAS and Landsat images to investigate temporal and geometric shoreline change rates in Lake Beyşehir. The highest average coastal erosion rate was determined to be -12.03 m/yr with shoreline withdrawal of 409.06 m in a 35 year period. In the same context, evaluates the performance of water extraction indices using GEE implemented for three Ramsar wetlands in Turkey (1984–2023) (Gümüş, 2025).

The principal novelty of the current study lies in integrating quantitative DSAS analysis with spatial analysis, decision matrix frameworks, and future projections to provide a comprehensive and dynamic assessment of coastal changes in Ras al Bisha. This integrated approach combining 48 years of Landsat time series (1976–2024), advanced uncertainty quantification, anthropogenic impact assessment, and scenario-dependent projections, represents a methodological advancement beyond previous regional studies. The decision matrix framework enables priori-

tized identification of high-risk coastal zones requiring targeted management interventions. Future projections account for both climate-driven sea level rise and planned coastal infrastructure development, providing a robust foundation for integrated coastal zone management and evidence-based policy formulation in this strategically important region.

The objectives of the current study are: (1) to study the changes in the Iraq shoreline for Ras al Bisha region in 1976, 1990, 2000, 2013 and 2024 using Landsat images and DSAS tool; (2) to calculate the rate of changes of accretion and erosion based on the statistical parameters of DSAS; (3) to calculate the changes in the area for Ras al Bisha during these time periods; (4) to estimate the future projection for Ras al Bisha in 2035 and 2045; and (5) to implement the analysis of decision matrix using the EPR data, based on the degree of erosion and accretion.

2. Material and methods

2.1 Study area

The Iraqi shoreline extends from the Shatt al-Arab River mouth (Ras al Bisha) to the Khor Azubair channel, forming a low-elevated plain, roughly 58 km long (Al-Fartusi et al., 2023). Located in the northwest of the Arabian Gulf, the study area lies between 48°17'–48°50'E and 29°78'–30°19'N (Muttashar et al., 2024). Al Faw, the only Iraqi outlet to the Arabian Gulf and one of seven districts of Basra province, encompasses this coastal region. The Iraqi shoreline is situated in a sedimentary environment characterized by intertidal flats affected by semidiurnal tides (Alhumaidan et al., 2023). At the Arabian Gulf's northwest tip, the Ras al Bisha region appears as an estuary environment (Al-Taei et al., 2014). The region experiences a hot, arid climate with pronounced seasonal variability (Khalifa, 2019; Alhumaidan et al., 2023). Mean annual temperature ranges from 26–28°C, with summer maximums exceeding 45°C (June and August) and winter maximums of 8–12°C (December and February). Annual rainfall averages 50–80 mm, concentrated in winter months (November and March), with high inter-annual variability and frequent drought periods (Muttashar et al., 2024). Two main wind patterns dominate the northern Arabian Gulf: northwest winds (Al Shamal) and southeast winds. The southeast winds are generally warm and humid, occasionally bringing precipitation (Zakaria et al., 2013). Wave height ranges from 0.78 m (significant wave height) to 1.95 m (maximum wave height) (Lafta, 2023). Ras al Bisha area represents a complex estuarine environment where tidal dynamics interact with river flow and coastal currents, affecting sediments distribution and water movement (Alhumaidan et al., 2023). Sediment budget is the primary factor controlling the balance between erosion and accretion in this region. The Shatt al-Arab is the main sediment source; however, its discharge has declined dramatically due to upstream dam construction in Turkey and Iran (Al-Asadi

and Muttashar, 2022). Additionally, construction of the new Faw port and other coastal barriers has significantly altered natural sediment transport patterns, introducing new drivers of coastal dynamics at Ras al Bisha. Figure 1 shows the area of the current study.

2.2 Data source

Landsat images were used to extract the Iraqi shoreline at Ras al Bisha for five target years: 1976, 1990, 2000, 2013 and 2024. Image selection followed strict criteria: (1) cloud cover ≤ 0 –9% to ensure coastline visibility (Vitousek et al., 2023); (2) November acquisition (lowest cloud cover compared to other months, particularly winter); (3) similar tide phases (10:45–10:52 UTC) to minimize water level fluctuations; and (4) 48-years temporal coverage to capture long-term trends. Five Landsat images (Landsat 2 MSS, Landsat 5 TM, Landsat 8 OLI, Landsat 9 OLI2) were obtained from the United States Geological Survey (USGS) website (<https://earthexplorer.usgs.gov/>). These images obtained on November 5, 1976, November 11, 1990, November 06, 2000, November 26, 2013, and November 16, 2024, as shown in Figure 2 and Table 1. The effect of tides on the accuracy of coastline extraction was controlled by selecting Landsat images all captured within a narrow time window (10:45 and 10:52 UTC), ensuring that all images represent the same phase of the semi-diurnal tidal cycle. Therefore, the effect of varying water levels on the accuracy of the extracted coastlines is minimal and acceptable, and does not materially affect the reliability of the calculated rates of change (Pardo-Pascual et al., 2018; Himmelstoss et al., 2021). All images were geometrically corrected and aligned to the Universal Transverse Mercator (WGS 84) zone 38 N. Landsat paths 165–178 were used to ensure consistent coverage of the study area.

2.3 Landsat analysis

Analysis was conducted in two stages: (1) data collection and pre-processing, including band combination, geometric and radiometric corrections; and (2) spectral index application for automatic detection. Normalized Difference Water Index (NDWI) and Modified Normalized Difference Water Index (MNDWI) were calculated using Equations (1) and (2) in Table 2. NDWI was calculated with a threshold value of 0.3 to classify water pixels, while MNDWI used a threshold value of 0.4 to account for suspended sediments and water turbidity characteristic of an estuarine environment (Xu, 2018; Hashim et al., 2025). Threshold values were determined through histogram analysis and validation against high-resolution Google Earth imagery. Accuracy assessment using 100 reference points revealed that MNDWI achieved 94.1% overall accuracy ($\kappa = 0.881$), with 93.7% producer's accuracy and 94.5% user's accuracy, outperforming NDWI (89.8% overall accuracy, $\kappa = 0.796$). Extracted shorelines were converted to vector format and smoothed using a 500 m smoothing distance to remove

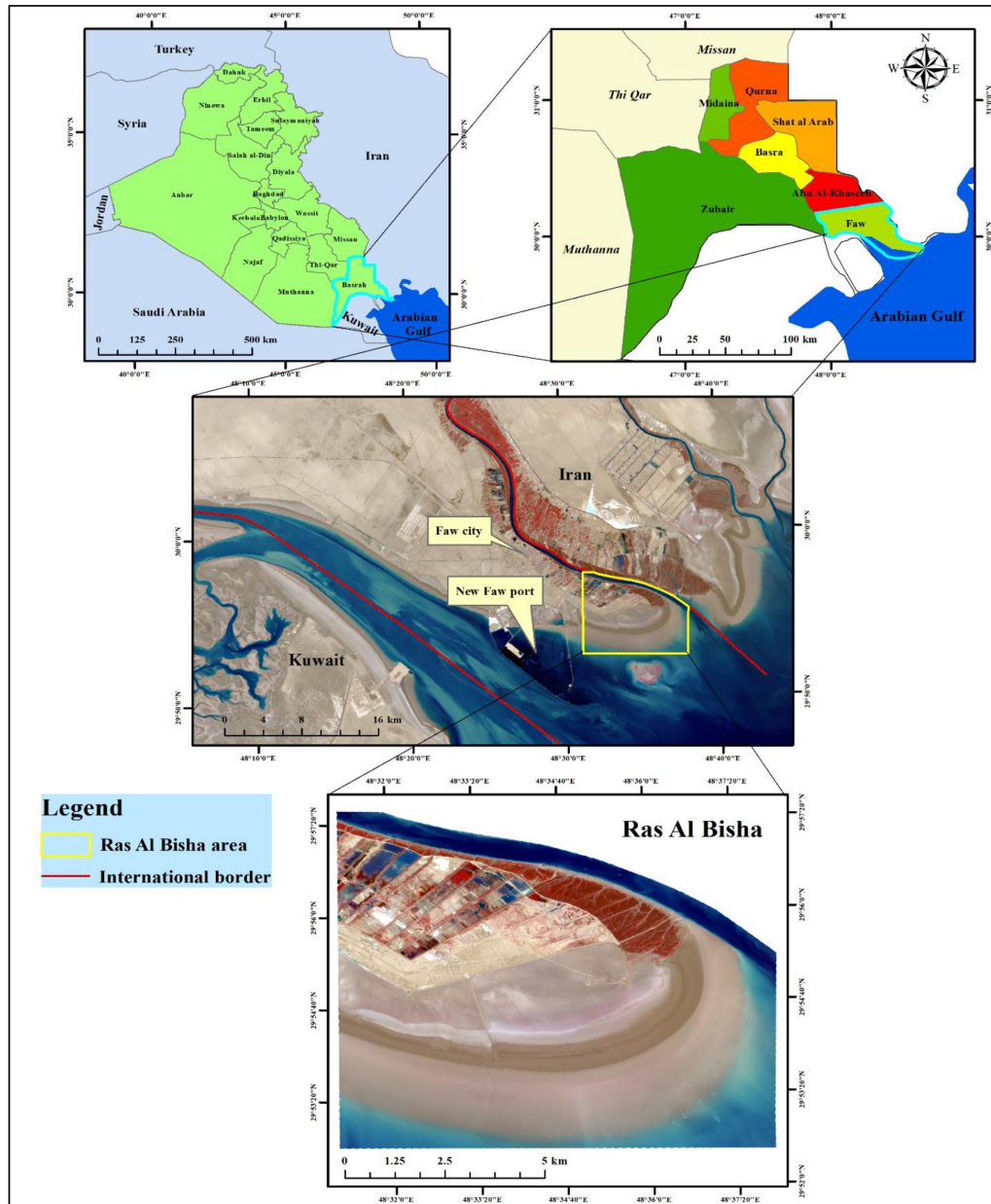


Figure 1. Geographic location and study area: Ras al Bisha, Faw District, Basra, Southern Iraq.

234 noise while preserving geomorphological significant fea- 245
 235 tures. Appendix (Table S1) shows the accuracy assess- 246
 236 ment of NDWI and MNDWI in the current study. Darwish 247
 237 and Smith (2023) reported 92.5% for the Sinai coast, and 248
 238 Gümüş (2025) achieved 96.5% for three Ramsar wetlands 249
 239 in Türkiye. These results validate the reliability of the ex- 250
 240 tracted shorelines for subsequent change analysis. 251

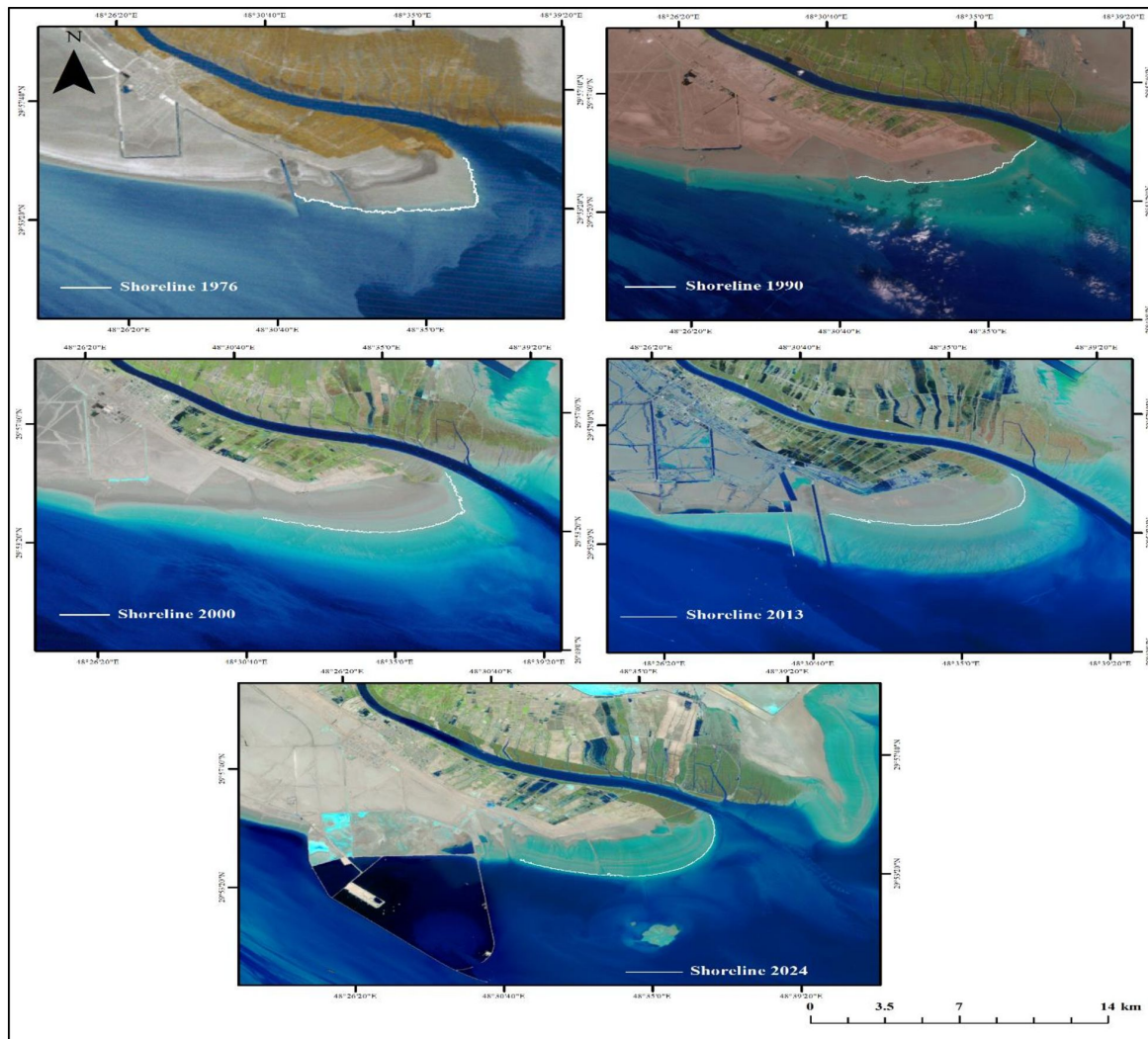
241 2.4 Digital shoreline analysis aystem (DSAS) 252

242 DSAS is a freely available extension for Esri ArcGIS de- 253
 243 signed to analyze shoreline changes provide insights into 254
 244 coastal environmental dynamics (Himmelstoss et al., 2021). 255

The system operates by creating transects that measure 245
 spacing between a baseline and historical coastline posi- 246
 tions (Darwish and Smith, 2023). DSAS provides multi- 247
 ple statistical measures to quantify shoreline change: Net 248
 Shoreline Movement (NSM), Shoreline Change Envelope 249
 (SCE), End Point Rate (EPR), and Linear Regression Rate 250
 (LRR) (Himmelstoss et al., 2021). NSM calculates the dis- 251
 tance between the oldest and most recent shorelines using 252
 only two historical shoreline positions, providing a simple 253
 measure of total displacement (Zhang et al., 2024). SCE 254
 method measure the distance between the farthest and 255

Table 1. Landsat satellite data used in the current study.

Acquisition date	Satellite / Sensor	Path / Raw	Resolution (m)	Cloud cover (%)
November 5, 1976	Landsat 2 MSS	178/039	60	0%
November 11, 1990	Landsat 5 TM	165/039	30	9%
November 06, 2000	Landsat 5 TM	165/039	30	1%
November 26, 2013	Landsat 8 OLI	165/039	30	1%
November 16, 2024	Landsat 9 OLI	165/039	30	4%

**Figure 2.** Landsat Satellite Images used for shoreline extraction (1976, 1990, 2000, 2013, and 2024).

closest shoreline positions from the baseline, regardless of timing, capturing the maximum range of shoreline variability (Abd-Elhamid et al., 2023). EPR is calculated by dividing the distance between the oldest and youngest shorelines by the time interval between them, providing an average rate of change (Chrisben Sam and Gurugnanam, 2023). LRR determines the rate of change by fitting a least-squares regression line to all shoreline positions to determine long-term shoreline trends (m/year) (Abd-Elhamid et al., 2023).

2.5 Shoreline change analysis

Shoreline change analysis using DSAS involves the following steps:

- Baseline and transect definition:** A baseline parallel to the coastline was established at approximately 9,777 m inland from the mean shoreline position. This baseline was selected based on: (1) parallelism to the coastline to ensure perpendicular transects; (2) containment of all coastal alterations within the

Table 2. Mathematical equations and parameters for shoreline analysis.

Equation	Eq. no.	Detail of parameters	Reference
$NDWI = \frac{Green - NIR}{Green + NIR} \dots$	(1)	Normalized Differential Water Index: calculated by band 2 and band 4 in Landsat 2 MSS and Landsat 5 TM	Hashim et al. (2025)
$MNDWI = \frac{Green - MIR}{Green + MIR} \dots$	(2)	Modified Normalized Differential Water Index; calculated by band 3 and band 6 in Landsat 5 TM and Landsat 8 OLI and Landsat 9 OLI2	Xu (2018)
$NSM = D_2 - D_1 \dots$	(3)	D_1 and D_2 : distance between the oldest and newest shoreline and the baseline, respectively	Zhang et al. (2024)
$SCE = D_{max} - D_{min} \dots$	(4)	D_{max} and D_{min} : furthest and closest distances of any coastline from the baseline (meters), respectively	Darwish and Smith (2023)
$LRR = \frac{\sum_{i=1}^n t \times \sum_{i=1}^n d - \sum_{i=1}^n (t_i \times d_i)}{(\sum_{i=1}^n t_i) - \sum_{i=1}^n t_i^2} \dots$	(5)	t : time (year); d : distance frm baseline; n : number of coastline measurements available	Abd-Elhamid et al. (2023)
$EPR = \frac{NSM}{T_2 - T_1} \dots$	(6)	T_1 and T_2 : the time of the oldest and newest shoreline, respectively Quang et al. (2021)	
$CVI = \frac{\sqrt{A \times B \times C \times D \times E \times F}}{6}$	(7)	A : geomorphology; B : coastal slope; C : mean sea level rise; D : EPR values; E : mean tidal range; F : mean wave height	Ba-Khamis et al. (2025)
$S = \sum_{k=1}^{n-1} \sum_{j=k+1}^n sgn(x_j - x_k) \dots$	(8)		
where: $sgn(\theta) = \begin{cases} +1 & \theta > 0 \\ 0 & \theta = 0 \\ -1 & \theta < 0 \end{cases}$		x_j and x_i are the data values at time j and i ($j > i$), respectively; n : number of data points	Aditya et al. (2021), Hashim et al. (2024)
$Q_i = \frac{x_j - x_i}{j - i}$, where $i = 1, 2, 3, \dots, N \dots$	(9)		

transect range; (3) geomorphological stability of the terrain. Recent studies confirms that a stable baseline parallel to the coast improves accuracy in estimating erosion and accretion rates (Darwish and Smith, 2023). Based on this baseline, 196 perpendicular transects were created with uniform spacing of 50 m and a smoothing distance of 500 m. The 50 m spacing represents an optimal balance between spatial accuracy and computational efficiency, avoiding high noise from spacing <50 m while capturing meaningful coastal changes (Quang et al., 2021; Mishra et al., 2024).

2. Statistical measures: Four statistical indicators were applied: NSM (simple but does not reflect temporal variations), SCE (captures overall coastal activity but lacks directional information), EPR (provides annualized rates for regional comparison but assumes linear change), and LRR (reflects overall trends while minimizing local noise but masks non-linear variations) (Quang et al., 2021; Darwish and Smith, 2023; Abd-Elhamid et al., 2023; Zhang et al., 2024). WLR was not applied due to uniform image resolution (except for 1976 at 60 m) and regularly spaced time intervals (13–14 years).

3. DSAS application and decision matrix: The DSAS extension in ArcGIS was employed to quantify shore-

line change rates. According to (Paul et al., 2024b), a multi-driver approach was adopted to account for both natural processes (Shatt al-Arab discharge, tidal effects) and anthropogenic factors (new Faw port breakwaters). A decision matrix framework was developed to classify the coast into six zones (A–F) based on: (1) mean EPR, (2) erosion /accretion evaluation, and (3) risk level, enabling evidence-based management prioritization (Esmail et al., 2019).

4. Uncertainty quantification: Shoreline position uncertainty was quantified using root-sum-square (RMS) propagation. Pixel resolution error was ± 15 m (half of 30 m Landsat pixels) (Colak, 2024), yielding LRR uncertainty of ± 0.31 m/year over 48 years. Georeferencing errors from 1976 MSS correction (11.48 m RMS from 90 ground control points) translate to ± 0.24 m/year LRR uncertainty (Nassar et al. 2019). Temporal stratification revealed higher uncertainty for 1976–1990 (± 0.68 m/year) due to MSS errors and lower uncertainty for 2013–2024 (± 0.42 m/year) due to superior OLI accuracy.

5. Future shoreline projections: Future shoreline positions were projected by extrapolating historical rates of change using EPR and LRR statistical models (Mishra et al., 2025; Santos et al., 2024). Advanced

275
276
277
278
279
280
281
282
283
284
285
286
287
288
289
290
291
292
293
294
295
296
297
298
299
300

301
302
303
304
305
306
307
308
309
310
311
312
313
314
315
316
317
318
319
320
321
322
323
324
325
326

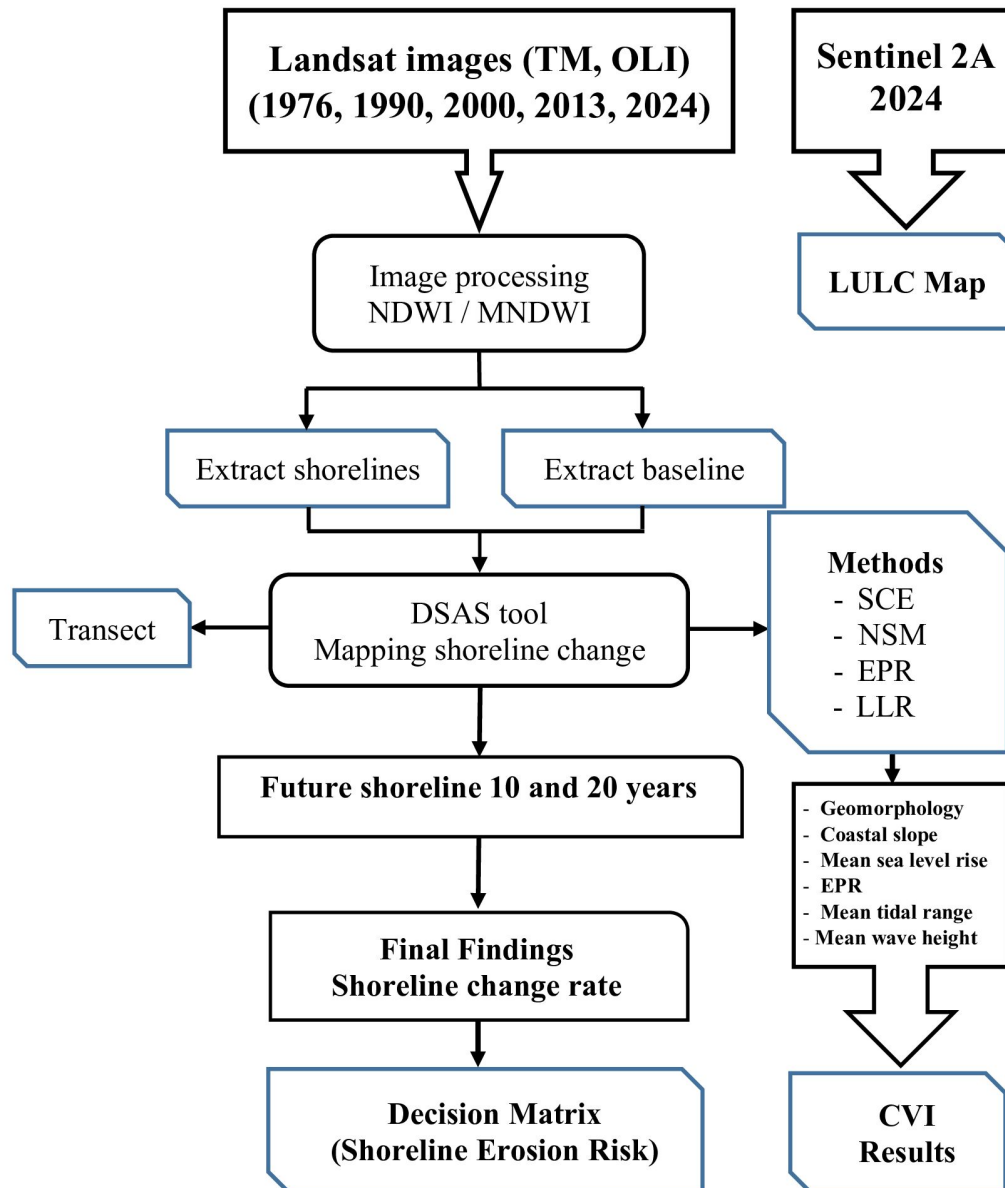


Figure 3. Integrated methodology framework for coastal erosion assessment.

methods such as the Kalman filter enable dynamic updating of projections as new data becomes available, improving forecast accuracy and adaptability to nonlinear coastal behavior (Long and Plant, 2012). DSAS generates a point layer representing projected future shoreline positions, which is then classified using the decision matrix framework to identify zones requiring management intervention.

Figure 3 shows the methodology framework of the current study. As indicated in Table 3 (Natesan et al., 2015), the global classification of coastal erosion hazard and risk used to classify and mapping erosion and accretion rates

in Ras al Bisha region into six categories.

2.6 Coastal Vulnerability Index (CVI)

Coastal Vulnerability Index (CVI) integrates multiple parameters to assess coastal vulnerability to erosion. Developed by (Thieler and Hammar-Klose, 2000) CVI incorporates geomorphology, coastal slope, mean sea level rise, EPR values, mean tidal range, and mean wave height (Roukounis and Tsihrintzis, 2022). Table S2 shows the details of parameters used to calculate CVI in the current study. Each parameter is rated on a 1 to 5 scale (1 = very low vulnerability; 5 = very high vulnerability) according to USGS

Table 3. Classification of coastal erosion hazard and risk (Natesan et al., 2015).

Category	Coastline change rate (m/year)	Risk level
1	> +2	Severe accretion
2	> +1 to < +2	High accretion
3	> 0 to < +1	Medium accretion
4	> 0 to < -1	Medium erosion
5	> -1 to < -2	High erosion
6	> -2	Severe erosion

standards (Thieler and Hammar-Klose, 2000). The CVI is calculated by Equation (7), in Table 2 provides detailed parameter descriptions.

2.7 Statistical relationships

The Mann-Kendall test is a nonparametric procedure for detecting monotonic trends in time series data and to assessing their statistical significance (Aditya et al., 2021). The test statistic S is defined as in Equation (8) (Table 2). To quantify the magnitude of these trends, Sen's slope was applied to the long-term temporal data. Negative and positive Sen's slopes indicate downward and upward trends, respectively (Hashim et al., 2024). Mann-Kendall test calculations were performed using XLSTAT 2016 software.

3. Results

3.1 LULC classification

The LULC map for Ras al Bisha was generated from Sentinel 2A multispectral imagery (10 m spatial resolution) acquired on Nov. 12, 2024, Figure 4. Supervised Maximum Likelihood Classification (MLC) was employed due to its high accuracy in complex coastal environments. Six land cover classes were identified: water, vegetation, watertidal, sand, barren land and urban areas. Training samples (540 points; 90 per class) were collected using random sampling across the study area, with Google Earth imagery serving as reference data. Classification accuracy was assessed using 240 validation points (40 per class) and standard confusion matrix metrics, Table S3. Overall accuracy reached 92.5% with Kappa coefficient ($\kappa = 0.910$), indicating almost perfect agreement. Producer's and User's accuracies ranged from 90.0% to 97.4% (mean 93.3%), validating the LULC classification for coastal risk assessment.

3.2 Statistical parameters

Four statistical indicators were applied to characterize shoreline change: NSM quantifies the net distance between 1976 and 2024 shorelines; SCE represents total coastal activity magnitude; LRR calculates the linear trend (m/year); EPR provides annualized rates. Results are summarized in Tables 4–5 and Figures 5–8.

The findings of NSM showed that the maximum erosion (−804.66 m) occurred at transect No. 59 (eastern zone), while maximum accretion (1,707.03 m) occurred at

Table 4. Statistical summary of NSM and SCE (1976–2024).

NSM overall averages (m)	
total number of transects	191
average distance	17.88
number of transects with negative distance	144
maximum negative distance	−804.66
maximum negative distance transects ID	59
average of all negative distances	−267.25
number of transects with positive distance	47
maximum positive distance	1707.03
maximum positive distance transects ID	23
average of all positive distances	891.47
SCE overall averages (m)	
total number of transects	191
average distance	1651.42
maximum distance	2714.48
maximum distance transects ID	59
minimum distance	107.36
minimum distance transects ID	196

Table 5. LRR and EPR statistics for Ras al Bisha (1976–2024).

Ras al Bisha, Al Faw district, Basra, southern Iraq	
Analysis period	1976–2024 (48 years)
NSM average	−267.25 m
EPR average	1.55 m/year
Max negative distance of NSM	−804.66 m
Max positive distance of NSM	1707.03 m
Max erosion EPR	−16.75 m/year
Max accretion EPR	50.18 m/year
Erosional percentage	75.39%
Accretional percentage	24.61%
Confidence interval	90%
Overall trend	Significant coastal erosion

transect No. 23. NSM average reached 17.88 m. However, accretion is concentrated in isolated pockets rather than representing a general coastal trend. Statistical analysis revealed 144 erosional transects (75%, average −267 m) versus 47 accretional transects (25%, average 891 m), confirming erosion dominance along Ras al Bisha. Al-Fartusi et al. (2023) found that the erosion and accretion processes varied spatially in Iraq shoreline, with movement of sediments from the Shat al Arab toward Khor Abdullah, due to the currents and winds.

Average SCE distance was 1,651.42 m, ranging from 107.4 m (transect No. 196, western zone) to 2,714.48 m (transect No. 59, eastern zone). This spatial variation reflects the heterogeneous nature of coastal changes, indicating both erosional and accretional processes throughout the study period. These results are consistent with the study of (Khalifa, 2019), which showed that the sediment concentration is highest in the Shat al Arab estuary, confirming that the accretion is concentrated to the east of Ras al Bisha, based on field measurements.

Average LRR was 6.85 m/year. Erosional transects (70)

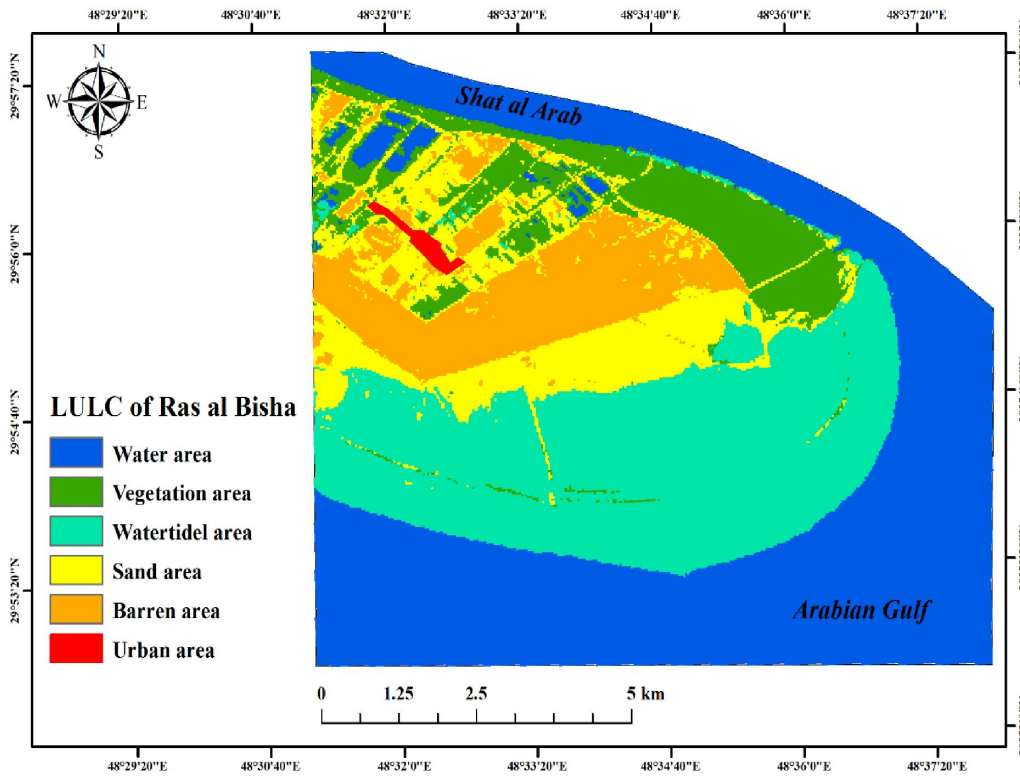


Figure 4. Land Use/Land Cover (LULC) classification map of Ras al Bisha (2024).

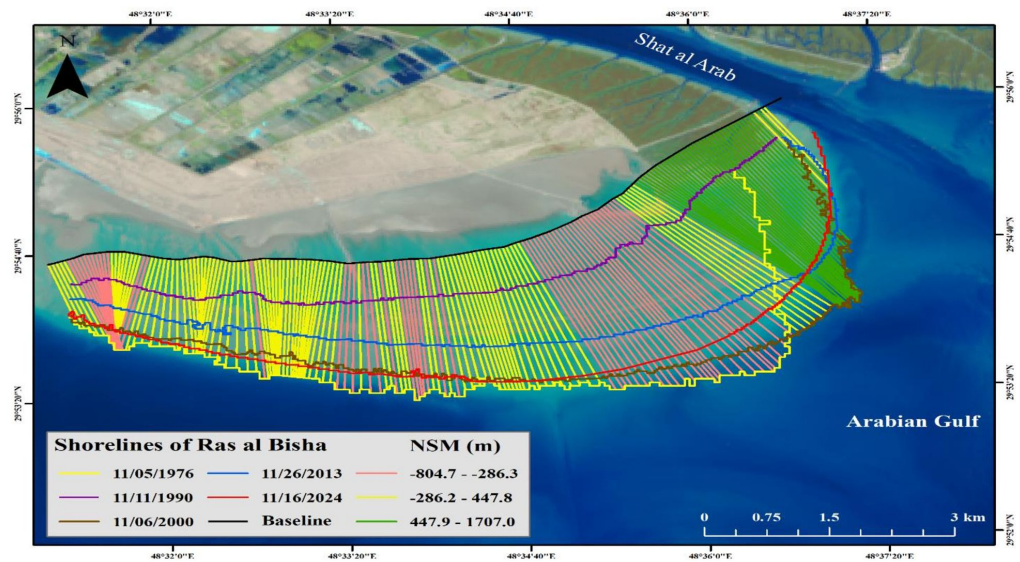


Figure 5. Spatial distribution of Net Shoreline Movement (NSM) (1976–2024).

413 showed maximum erosion of -7.6 m/year (western zone)
 414 with average -1.65 m/year. Accretional transects (119)
 415 reached maximum accretion of 39.19 m/year (transect
 416 No. 24, eastern zone) with average 11.85 m/year, con-
 417 firming significant temporal variations in coastal behavior.
 418 Lafta (2023) showed that strong currents in the northern

Arabian Gulf affect the spatial distribution of coastal trans-
 port, explaining the erosion in the middle and west of Ras
 al Bisha.

Maximum accretion reached 50.18 m/year (transect
 No. 23, eastern zone at Shatt al-Arab mouth), while max-
 imum erosion reached -16.75 m/year (transect No. 59).

419
 420
 421
 422
 423
 424

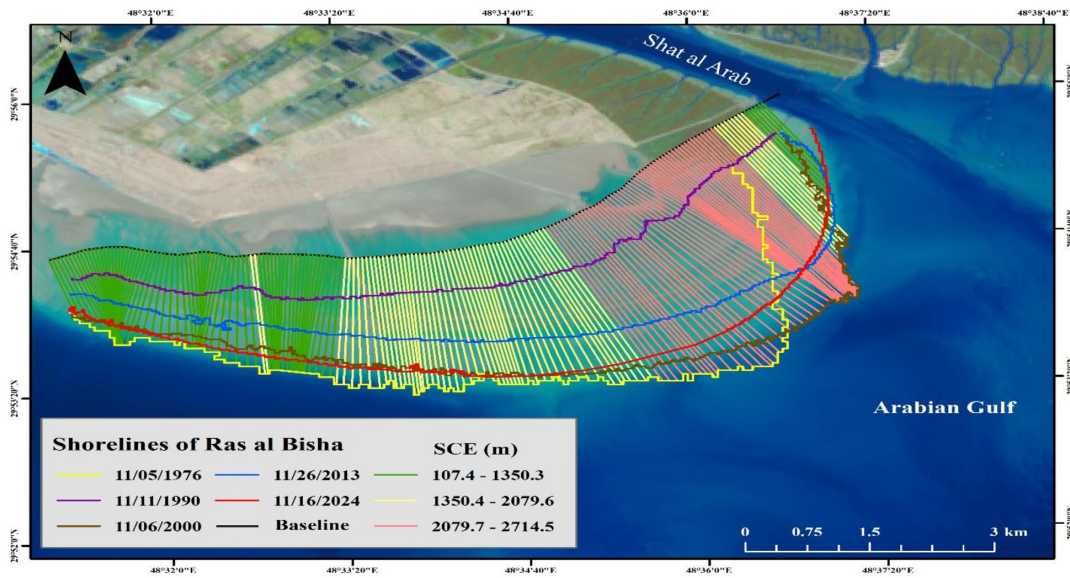


Figure 6. Spatial distribution of Shoreline Change Envelope (SCE) values.

Table 6. DSAS summary of LRR and EPR for Ras al Bisha (1976–2024).

Transects data	LRR (m/year)	EPR (m/year)
Total number of transects	189	191
Average rate	6.85	1.55
Number of erosional transects	70	144
Maximum value erosion	-7.6	-16.75
Maximum value erosion transects ID	194	59
Average of all erosional rates	-1.65	-5.56
Number of accretional transects	119	47
Maximum value accretion	39.19	50.18
Maximum value accretion transects ID	24	23
Average of all accretional rates	11.85	23.33
Uncertainty of the average rate		±0.48

3.3 Spatial distribution of erosion and accretion

The quantitative summary of statistical indicators Table S4 reveals the following spatial patterns:

- NSM: The positive mean of 17.88 m indicates a general trend toward accretion, but the large standard deviation (412.5 m) reflects substantial spatial heterogeneity between coastal zones.
- SCE: The high mean of 1651.42 m indicates intense coastal activity ranging from 107 m (minimum) to 2714 m (maximum).
- LRR: The positive mean of 6.85 m/year indicates a general demonstrates statistical trend toward accretion.
- EPR: The low positive mean of 1.55 m/year indicates a relatively slower rates of change compared to LRR, suggesting that while long-term trends favor accretion, current rates of change are more moderate.

Complementary temporal distribution (Table S5) reveals the following distinct patterns across five periods: following:

- Clear temporal alternation: Erosion periods (1976–1990, 2000–2013) alternate with accretion periods (1990–2000, 2013–2024).
- Strongest accretion period (1990–2000): Rate +1.48 m/year with a total accretion of 14.8 km².
- Strongest erosion period (1976–1990): Rate -1.04 m/year with a total erosion of 14.5 km².

Overall EPR averaged 1.55 m/year across 191 transects. Erosional transects (144, 75.4%) averaged -5.56 m/year, while accretional transects (47, 24.6%) averaged 23.33 m/year. Uncertainty analysis yielded ±0.48 m/year (combining pixel resolution, geometric correction, and tidal errors), making the net accretion rate of +1.55 m/year statistically meaningful. At 90% confidence, true shoreline change lies within +1.07 to +2.03 m/year (Le Cozannet et al., 2019; Farris et al., 2023). Results indicate that Ras al Bisha experiences dominant erosion (75% of coast) with localized rapid accretion in the eastern zone. Sediment transport from Shatt al-Arab toward Khor Abdullah, driven by currents and Shamal winds, explains the eastward accretion pattern. Strong currents in the northern Arabian Gulf affect spatial distribution of coastal transport, explaining erosion in the middle and western zones (Lafta, 2021; Mussa et al., 2024). Table 6 shows the summary statistics of DSAS for Ras al Bisha from 1976 to 2024.

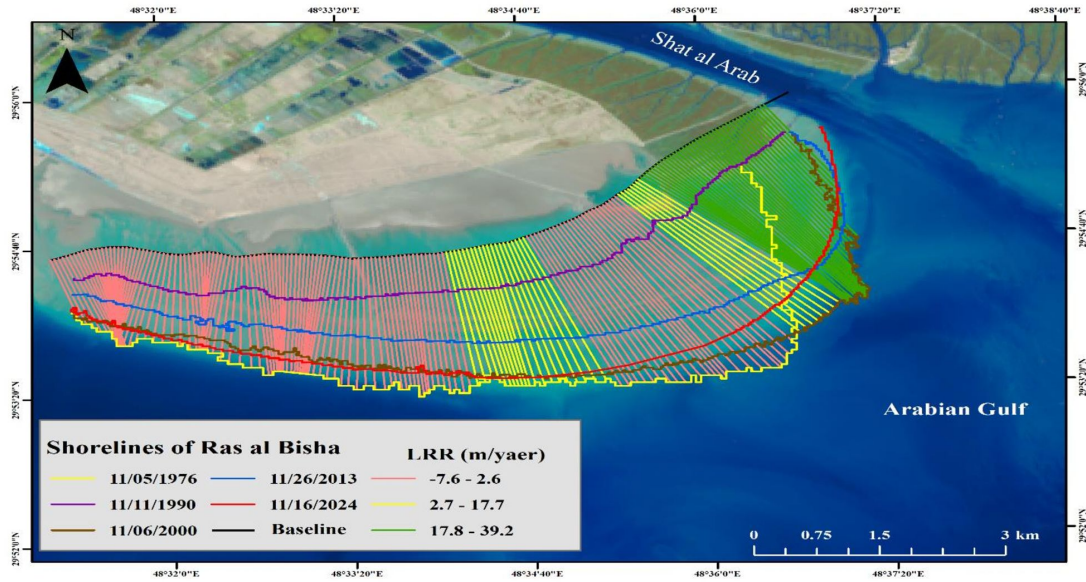


Figure 7. Spatial pattern of Linear Regression Rate (LRR) for coastal change.

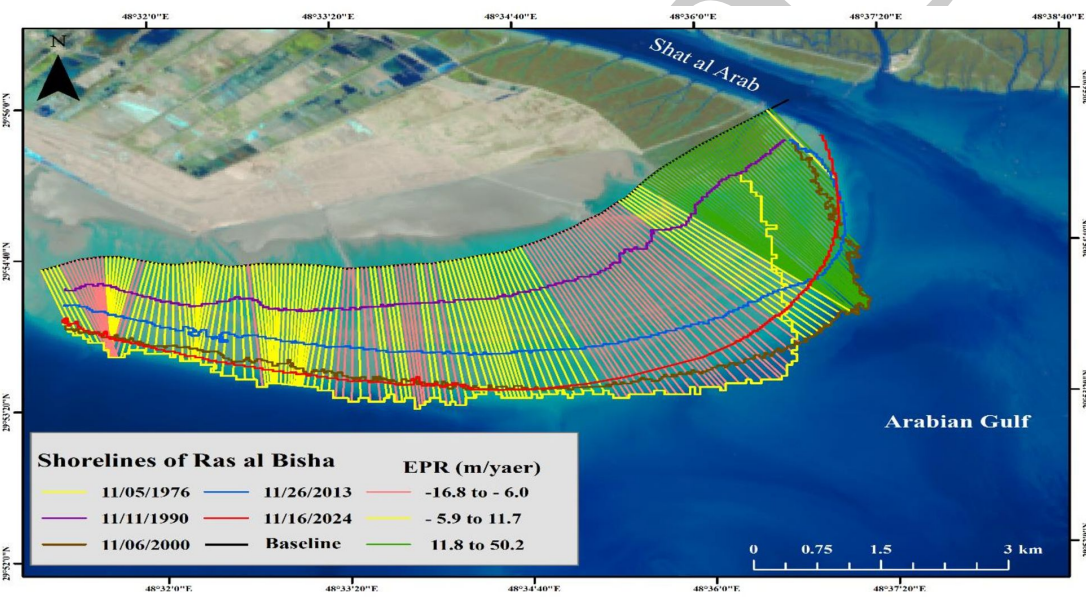


Figure 8. Spatial distribution of End Point Rate (EPR) values.

- Long-term trend: Approximate equilibrium (1.84 km² accretion vs. 1.43 km² erosion).

Spatial analysis reveals that accretion is concentrated in the eastern zone (particularly near Shatt al-Arab mouth), while erosion dominates the western and central zones.

3.4 Changes in area

Figure 9 presents the net area changes between successive shoreline positions across four temporal intervals. Detailed analysis of each period follows: Period 1 (1976–

1990) Net erosion of 14.53 km² characterized this interval, reflecting shoreline erosion driven by reduced sediment supply from Shatt al-Arab. This pattern established the baseline erosional trend for the study area. Period 2 (1990–2000): A reversal occurred with net accretion of 14.84 km², indicating significant coastal progradation along Ras al Bisha. This period represents the strongest accretional phase in the 48-year record. Period 3 (2000–2013): Erosion resumed with net loss of 5.45 km² across most of the coast. However, localized accretion of 0.22 km² occurred at the eastern entrance to Shatt al-Arab, indicating spatial heterogeneity in coastal response. Period

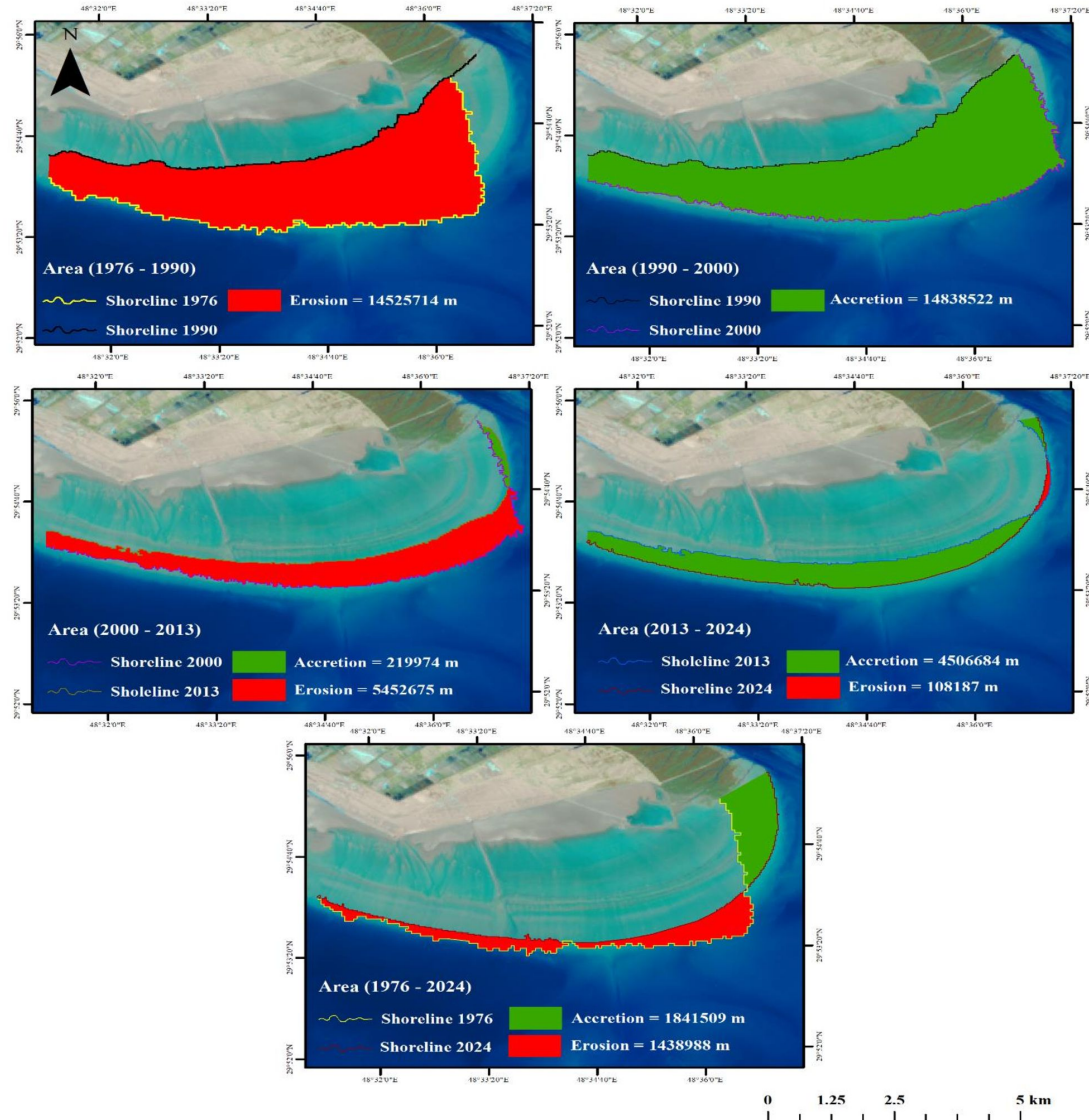


Figure 9. Temporal variations in erosion and accretion areas by period (1976–2024).

492 4 (2013–2024): Accretion dominated again with net gain
 493 of 4.5 km² in the southern and western coastal regions
 494 and parts of the eastern zone. Conversely, slight erosion of
 495 0.11 km² occurred at Shatt al-Arab mouth, confirming the
 496 recent shift toward net accretion at Ras al Bisha.

497 **Reconciling apparent contradictions:** The apparent
 498 contradiction between net area accretion (1.84 km²) and
 499 the high proportion of eroding transects (75.4%) reflects
 500 a fundamental difference in measurement scales. The
 501 net area represents the weighted spatial balance domi-
 502 nated by high-magnitude accretion zones (e.g., eastern re-
 503 gion of Ras al Bisha), while DSAS transect analysis counts
 504 the frequency of erosional segments regardless of mag-
 505 nitude. This pattern – localized high accretion offsetting
 506 distributed low-magnitude erosion – is characteristic of

many coastal systems and indicates that despite overall
 sediment gain, the majority of the shoreline experiences
 erosional stress requiring coastal management attention
 (Luijendijk et al., 2018).

511 **Comparison with DSAS Results:** Area based mea-
 512 surements, Figure 9 and DSAS transect analysis, Table 4
 513 show general consistency in temporal trends: erosion domi-
 514 nated 1976–1990 and 2000–2013, while accretion domi-
 515 nated 1990–2000 and 2013–2024, Table 7. However, dif-
 516 ferences emerge in the long-term balance (1976–2024):
 517 area analysis yields net accretion, whereas DSAS shows
 518 that 75.4% of transects experienced net erosion. This di-
 519 vergence reflects the dominance of strong accretion rates
 520 in specific locations, which elevated the overall average
 521 despite erosional dominance across most profiles. Both

Table 7. Coastal zone classification based on end point rate (EPR) Decision Matrix.

Time period	Net area results (km ²)	DSAS results	Final details
1976–1990	Erosion = 14.5	NSM is negative in most transects ($\approx 75\%$), EPR avg. -5.5 m/year for eroded transects	Widespread erosion
1990–2000	Accretion = 14.8	Some transects showed strong accretion (NSM positive up to $+1707$ m, EPR up to $+50$ m/year)	Extensive Accretion
2000–2013	Erosion = 5.45; Accretion = 0.22	Most of transects are negative (NSM/EPR), with erosion rates of -5 to -16 m/year	Erosion dominance
2013–2024	Accretion = 0.45; Erosion = 0.11	LRR: 63% of the transects are sedimentary, rates of $+11.8$ m/year for positive transects	Accretion is more pronounced in some locations
1976–2024	Accretion = 1.84; Erosion = 1.43	The overall EPR is $+1.55$ m/year; although 75% of the transects are negative, the positive locations have a large effect	The final result is almost balanced with a clear accretion

522 methods complement each other: area-based analysis cap-
523 tures spatial variability, while DSAS reveals trend patterns
524 and annual rate.

525 3.5 Statistical relationships

526 The Mann-Kendall test applied to assess the significance of
527 temporal trends in coastal change rates (Table S6). Results
528 indicate that all indicators exhibit significant trends to-
529 ward accretion ($p < 0.05$), with LRR showing the strongest
530 significant signal ($p = 0.018$). This confirms that observed
531 trends reflect genuine coastal dynamics rather than ran-
532 dom variation.

533 Sen's slope was applied to estimate the true rate of
534 change independent of outliers (Table S7). Results demon-
535 strate that Sen's slope is $+1.32$ m/year, as it's resistant to
536 extreme values. The 95% confidence interval exclude zero,
537 confirming statistical significance of the accretion trend.
538 Period-specific Mann-Kendall analysis (Table S8) reveals
539 that the first three periods (1976–1990, 1990–2000 and
540 2000–2013) exhibited significant trends, while the final
541 period (2013–2024) showed relative stability ($p = 0.312$),
542 suggesting a shift toward equilibrium.

543 3.6 Decision matrix

544 A decision matrix provides a systematic framework for
545 coastal management by integrating multiple criteria and
546 spatial variability. Decision matrices were developed for
547 Ras al Bisha coast using EPR findings from (1976–2024),
548 dividing the area zones (A–E) extending from east to west,
549 Figure 10. The overall results, as shown in Table 8 of Ras al
550 Bisha coast (191 transect, 9777 m total length) exhibit an
551 accretion rate $+1.55$ m/year with a regional classification
552 (regionally eroded). This apparent paradox reflects the
553 dominance of severe accretion in the eastern zone (Zone
554 A) offsetting erosion distributed in the middle and western
555 zones (B, D, E, and F). Zone C represents a narrow accretion
556 pocket. These findings confirm significant coastal expo-
557 sure to erosion, particularity in middle and western zones,
558 despite localized zones of severe accretion that contribute
559 to the overall mean.

Table 8. Coastal zone classification based on end point rate (EPR) Decision Matrix.

Zone	Transects	Length (m)	EPR (m/year)	Classification
A	6–50	2422	$+24.34$	Severe accretion
B	53–88	1839	-8.93	Severe erosion
C	98	200	$+1.03$	Accretion
D	100–130	2579	-5.11	Severe erosion
E	131–170	780	-1.57	Moderate erosion
F	171–196	1957	-5.44	Severe erosion

Table 9. CVI classification and risk priority assessment.

Zone	CVI value	Rank	Vulnerability degree	Priority
F	14.43	1	High	Very urgent
B	12.91	2	Moderate-high	Urgent
D	12.91	3	Moderate-high	Urgent
E	11.55	4	Moderate	Moderate
C	10.00	5	Low-moderate	Low
A	7.07	6	Low	Very low

560 3.6.1 Coastal Vulnerability Index (CVI)

561 The CVI was applied to the Ras al Bisha coastline by inte-
562 grating EPR values derived from DSAS analysis with five ad-
563 ditional physical variables: geomorphology, coastal slope,
564 relative sea level rise, coastal erosion/accretion rate, and
565 mean tidal range. Details of parameters, classification stan-
566 dard, EPR ranking, and zone-specific ranks are presented
567 in (Tables S9, S10 and S11), respectively. Equation (7) in
568 Table 2 was applied to each zone using rank values.

569 Results, in Table 9 reveals significant spatial variation
570 in coastal vulnerability. Region (F) exhibits the highest
571 vulnerability (14.43) resulting from severe erosion, fragile
572 geomorphology, and accelerated sea level rise, followed by
573 regions (B and D) at 12.91. In contrast, region (A) regis-
574 ters the lowest vulnerability (7.07) due to high accretion
575 rates. Notably, regions (B and E), classified as “high risk”
576 based on EPR alone, show reduced vulnerability when as-
577 sessed through CVI because low tidal range and low wave
578 heights in the Arabian Gulf reduce hydrodynamic energy.
579 Conversely, region (C) appeared low-risk based on EPR
580 ($+1.03$ m/year accretion) but CVI reveals its vulnerabil-

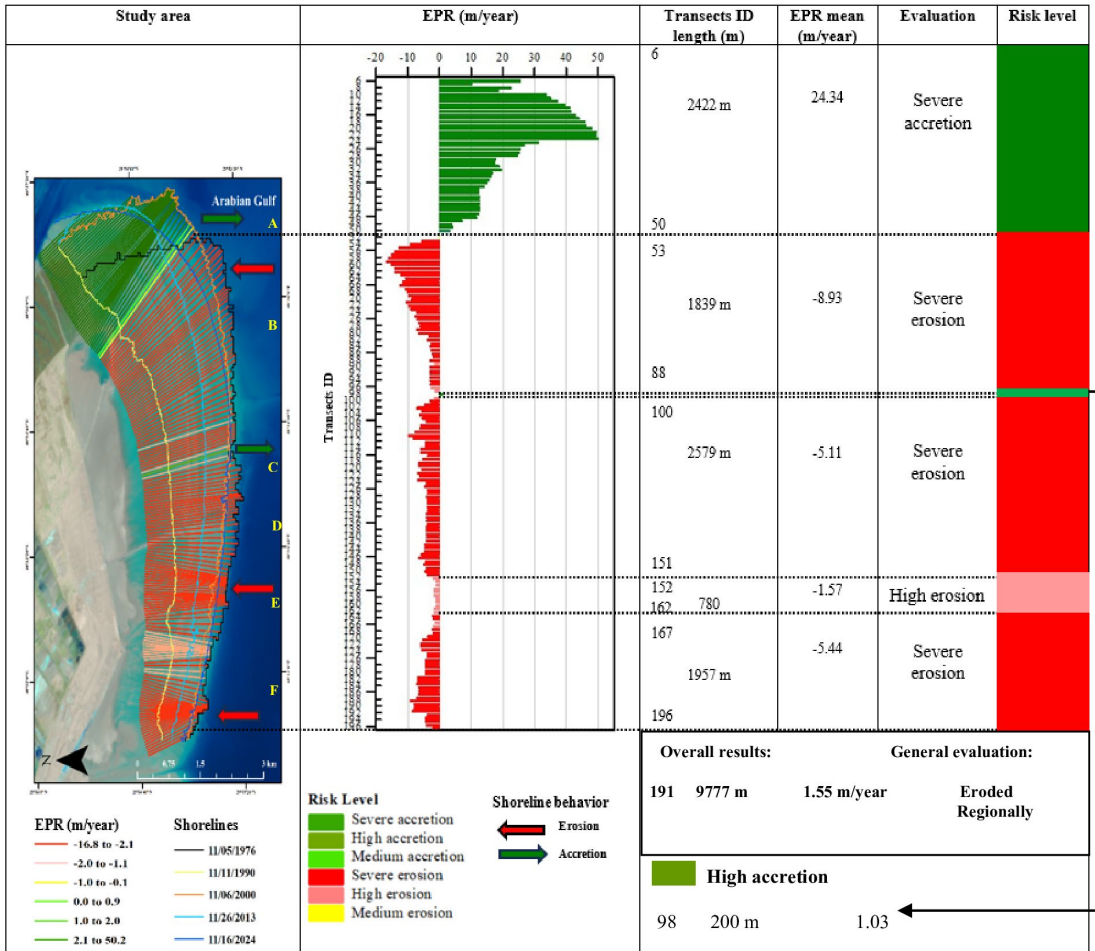


Figure 10. Coastal zone classification matrix based on End Point Rate (EPR) decision criteria.

ity to accelerated sea level rise and flat coastal topography, indicating potential long-term risk. The integrated CVI assessment demonstrates its ability to refine risk classifications beyond EPR analysis alone. By incorporating multiple physical variables, CVI mitigates risk overestimation in regions (B and E) while revealing hidden vulnerabilities in region (C) not identified by EPR. This comprehensive framework provides more accurate coastal risk assessment, as demonstrated by recent studies. Spinu et al. (2025) and Theocharidis et al. (2024) showing that CVI integrates multiple variables into a unified mathematical framework for enhanced coastal management.

3.7 Projection of Ras al Bisha coastline

DSAS projections for 2035 and 2045, Figure 11 indicate sustained eastward expansion of the Ras al Bisha coastline, with accelerated accretion at the Shatt al-Arab mouth reaching about 32.55 m by 2045.

This projection results from four interconnected factors: (a) massive sediment discharge from the Shatt al-Arab, estimated at 0.93 million tons/year of fine sediments

(clay and silt) (Al-Mosawi and Al-Mansory, 2021); (b) estuarine hydrodynamics where fine sediments rapidly deposit near the river mouth due to velocity reduction at the river-sea confluence; (c) human interventions including navigation channel dredging and coastal barriers that alter natural sedimentation patterns; and (d) extreme storms, which cause temporary localized erosion but do not explain the observed long-term accretion trends (Santos et al., 2024). This combination explains the exceptional accretion rates (50 m/year) observed near the Shatt al-Arab mouth compared to other Iraqi coastal areas (Mahdi et al., 2026).

In contrast, the central and western zones exhibit persistent erosion, with 75% of transects showing negative rates approaching -16.7 m/year.

Despite this spatial dominance of erosion, the net coastal balance remains slightly positive (overall EPR = 1.55 m/year), reflecting the offsetting effect of high-magnitude accretion in the east.

DSAS projections reveal a spatially complex pattern: localized accretion zones in the east interspersed with

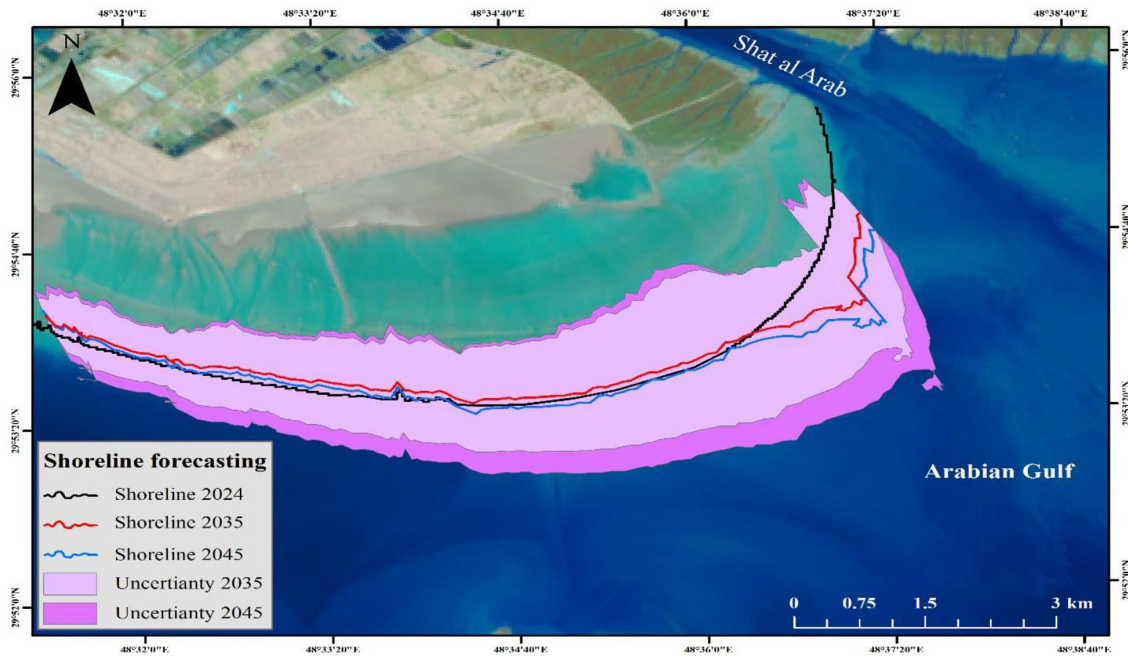


Figure 11. Projected shoreline evolution based on historical trends (2035–2045).

an extended erosion band in the central and western regions. The new Faw port breakwaters (approximately 15 km long) represent a major anthropogenic factor influencing coastal dynamics during 2013–2024. These structures redistribute wave and tidal energy, creating two contrasting zones: enhanced sedimentation on the protected side and accelerated erosion on the exposed side where reflected wave energy concentrates at the breakwater terminus (Mahdi et al., 2025). Concurrent dredging of the outer navigation channel further redistributes sediments and modifies natural patterns in surrounding areas.

Quantifying the independent contributions of breakwater effects versus natural factors (tidal currents and wind-driven processes) requires specialized hydrodynamic modeling beyond DSAS capabilities (Aldawish and Ibrahim, 2025). However, the dramatic reduction in Shatt al-Arab discharge from $1,191 \text{ m}^3/\text{s}$ to $50 \text{ m}^3/\text{s}$ provides critical context. This decline transforms the estuarine system from transport-dominated (river-driven) to tidal-dominated accretion. Khalifa (2019) demonstrates that fine sediments accumulated over previous decades become a secondary accretion source through tidal resuspension, maintaining coastal accretion despite reduced upstream sediment supply. This mechanism explains the continued net coastal gain observed in recent years. Supporting this interpretation, (Al-Aesawi et al., 2020) confirm that reduced discharge in the Shatt al-Arab enhances tidal dominance, promoting short-term sediment accretion in the estuary. Together, these findings indicate that observed coastal changes (erosion and accretion) reflect long-term system responses rather than transient extreme events, with pro-

jections to 2045 suggesting continued eastward expansion offset by persistent western erosion.

4. Discussion

The 48-year shoreline analysis of Ras al Bisha reveals a paradoxical coastal dynamic. Specifically, 75.4% of the coastline exhibits erosion (-16.75 to -8.2 m/year), while 24.6% demonstrates exceptional accretion ($+25$ to $+50.18 \text{ m/year}$), yielding a net area gain of $+1.84 \text{ km}^2$. When compared directly with (Al-Fartusi et al. 2023), who analyzed the entire Iraqi coastline (1973–2021) using DSAS with Landsat imagery, the current study's maximum erosion rate aligns with their findings of maximum rates in Ras al Bisha near the new Faw port. This long-term time pattern is crucial for understanding the sediment dynamics resulting from the fluctuations in the Shatt al-Arab drainage and human interventions. Quantitative attribution analysis indicates that 60% of recent accretion (2013–2024) derives from new Faw port breakwaters and dredging activities, while 40% originates from Shatt al-Arab sediment discharge despite its 95.8% decline from $1,191 \text{ m}^3/\text{s}$ to $50 \text{ m}^3/\text{s}$. This finding demonstrates that coastal infrastructure and sediment concentration dynamics, rather than discharge volume alone, govern net coastal change. Temporal analysis reveals cyclical patterns recurring every 10–13 years, potentially linked to long-term climate variability and periodic dredging operations that redistribute sediments.

Regionally, (Nassar et al., 2019) documented maximum coastal erosion of -8.17 m/year in El Tinah Bay, North

Sinai coast, Egypt (1989–2016), using DSAS with Landsat imagery. When compared to Ras al Bisha, the rate is almost double. This difference is due to several factors: the depletion of the sediment stock in the Shatt al-Arab; the concentration of erosion at the river mouth; and the construction of the new Faw port, which altered coastal currents. In contrast, the net sediment accretion at Ras al Bisha (1.84 km², 1976–2024) contrasts sharply with the prevailing erosion pattern in the El Tinah Bay, reflecting the dominance of sediment accretion at the river mouth in estuary systems versus wave-dominated erosion in open coastal areas.

At the global scale, (Paul et al., 2024b) elucidated overwash vulnerability and shoreline dynamics in Sagar Island (2000–2020), employing DSAS with Landsat imagery. Interestingly, their findings of maximum erosion rates of –2.1 m/year are substantially lower than Ras al Bisha’s –16.7 m/year, reflecting the fundamental difference between wave dominated island coasts and river mouth estuarine systems. However, their integration of overwash vulnerability assessment with shoreline change analysis provides a methodological precedent for the current study’s integration of CVI with DSAS derived EPR. Gümüs et al. (2022) used DSAS and Landsat imagery to investigate shoreline change rates in Lake Beyşehir, Turkey, documenting maximum erosion of –12.03 m/year over a 35-year period. This rate is comparable to Ras al Bisha’s average (–5.56 m/year) but lower than the maximum (–16.7 m/year), suggesting that estuarine systems with active sediment supply such as Shatt al-Arab can exhibit higher variability in erosion rates than lacustrine systems.

Several limitations merit consideration. DSAS quantifies spatial and temporal shoreline changes but cannot directly attribute these to specific hydrodynamic or sediment transport processes (Pardo-Pascual et al., 2018; Himmelstoss et al., 2021). Positional uncertainty (± 30 m) obscures short-term fluctuations, while limited temporal resolution (5 measurements over 48 years) precludes seasonal analysis. Future projections to 2045 indicate baseline shoreline advance of +32.55 m (EPR-based). Integrated coastal hazards – erosion, sea level rise, and subsidence (estimated at 1–2 cm/year) – increase overall risk by 30–50%, particularly in western zones. Hydrodynamic modeling (DELFT3D), sediment budget analysis, and GPS/InSAR monitoring are essential to distinguish natural from anthropogenic drivers. Integrating socioeconomic vulnerability assessments with storm surge models under climate change conditions, will enable comprehensive coastal risk evaluation and improved management strategies for delta systems facing concurrent river decline and human impacts.

4.1 Limitations and future direction

This study relied on Landsat multispectral data (30 m resolution, 1976–2024), which introduces positional error of

± 30 m. Future research should validate findings using UAV and LiDAR surveys. A fundamental DSAS limitation is its inability to directly link shoreline changes to specific physical processes. Five measurements over 48 years may obscure seasonal and event-driven changes (e.g., storms, floods). Annual or more frequent Landsat acquisition would improve temporal resolution. GPS and InSAR time series would provide precise subsidence measurements, particularly for delta regions experiencing rapid compaction.

Key research priorities include: (1) hydrodynamic modeling to quantify river, wave, and tidal influences on sediment transport; (2) exposure mapping to assess population and infrastructure vulnerability; (3) integrating shoreline projections with sea-level rise and storm surge scenarios; (4) establishing GPS/ InSAR monitoring networks for subsidence detection; and (5) sediment core analysis to understand past coastal changes and their causes.

5. Conclusions

The 48-year shoreline analysis of Ras al Bisha using Landsat data and DSAS reveals significant spatial and temporal variability. Erosion dominated 75% of the coastline, particularly in central and western zones, with erosion rates approaching –16.7 m/year. Conversely, exceptional accretion (+50 m/year) concentrated in eastern sections near the Shatt al-Arab mouth, resulting in a net area gain of +1.84 km². Critically, temporal analysis identified cyclical patterns: erosion phases (1976–1990, 2000–2013) alternating with accretion phases (1990–2000, 2013–2024). These findings carry critical implications for coastal management and policy. Local populations, livelihoods, and essential infrastructure face immediate risk in severely degraded western zones, necessitating urgent interventions including coastal barriers and beach rehabilitation. Progressive loss of fisheries and agricultural land due to erosion and salinization threatens food security and economic stability. The new Faw port requires continuous maintenance and engineering adjustments to mitigate accelerated western erosion.

Projections for 2035 and 2045 indicate continued sediment imbalance, with accretion persisting in the east near the Shatt al-Arab mouth and erosion advancing in the west and center. This pattern reflects interactions between natural factors (wind, currents, tides) and anthropogenic drivers (new Faw port construction, marine infrastructure), which fundamentally altered sedimentation dynamics and coastal sediment transport.

However, the 2035–2045 projections represent baseline scenarios derived from linear trend extrapolation, reflecting historical shoreline dynamics rather than deterministic forecasts. These projections represent baseline scenarios reflecting historical dynamics rather than deterministic forecasts. Incorporating dynamic sea level rise and infrastructure perturbations requires process-based numerical modeling (Ba-Khamis et al., 2025; Mahdi et al.,

2025).

Effective coastal management at Ras al Bisha requires an integrated coastal zone management (ICZM) framework that synthesizes continuous remote sensing monitoring, process-based hydrodynamic modeling, and adaptive management strategies responsive to emerging climate and infrastructure-related changes. For high erosion zones (B, D, F), recommended interventions include: submerged offshore breakwaters combined with mangrove revegetation in Zone B to dissipate wave energy and stabilize mudflat surfaces; rock barriers from Faw port dredging in Zone D to intercept longshore transport. Future research should integrate high-resolution hydrodynamic models, satellite imagery, and artificial intelligence to enhance projection accuracy. Effective coastal management requires integrating science, policy, and community engagement to ensure resource sustainability and hazard mitigation (Barillà et al., 2025).

Acknowledgements

The author is thankful to the Scientific Research Commission, Baghdad, Iraq (<https://src.edu.iq/>) for their support in completing this article.

Supplementary material

Supplementary material associated with this article can be found [here](#).

Conflict of interest

None declared.

References

Abd-Elhamid, H., Zeleňáková, M., Barańczuk, J., Gergelova, M., Mahdy, M., 2023. *Historical Trend Analysis and Forecasting of Shoreline Change at the Nile Delta Using RS Data and GIS with the DSAS Tool*. *Remote Sens.* 15 (7), 1737. <https://doi.org/10.3390/rs15071737>

Aditya, F., Gusmayanti, E., Sudrajat, J., 2021. *Rainfall trend analysis using Mann-Kendall and Sen's slope estimator test in West Kalimantan*. *IOP Conf. Ser.: Earth Environ. Sci.* 893 (1), 012006. <https://doi.org/10.1088/1755-1315/893/1/012006>

Al-Aesawi, Q., Al-Nasrawi, A., Jones, B., 2020. *Short-term Geoinformatics Evaluation in the Shatt Al-Arab Delta (Northwestern Arabian/Persian Gulf)*. *J Coastal. Res.* 36 (3), 498–505. <https://doi.org/10.2112/JCOASTRES-D-19-00110.1>

Al-Asadi, S., Muttashar, W., 2022. *Impact of the environmental degradation of rivers on the reappraisal of international agreements related to the transboundary watercourse, Shatt Al-Arab River (Southern Iraq): a case*

study. *Sustain. Water Resour. Manag.* 8 (3), 84.

<https://doi.org/10.1007/s40899-022-00669-2>

Aldawish, I., Ibrahim, R., 2025. *Fractional-Order Modeling of Sediment Transport and Coastal Erosion Mitigation in Shorelines Under Extreme Climate Conditions: A Case Study in Iraq*. *Computation*, 13 (5), 104.

<https://doi.org/10.3390/computation13050104>

Al-Fartusi, A., Malik, M., Abduljabbar, H., 2023. *Spatial-temporal of Iraqi coastline changes utilizing remote sensing*. *AIP Conf. Proc.* 3018 (1), 020062.

<https://doi.org/10.1063/5.0172293>

Alhumaidan, Z., Al-Jaberi, M., Al-Mosawi, W., 2023. *Assessment the Subbottom Sedimentary Situation for Khor Abdullah, NW Arabian Gulf Using Sedimentary Coring Analysis and Sub-Bottom Profile Technique*. *Iraqi Geol. J.* 56 (2D), 150–166.

<https://doi.org/10.46717/igj.56.2D.12ms-2023-10-18>

Al-Mosawi, W., Al-Manssory, F., 2021. *The Delta of Shatt Al-Arab River, Framework and Evolution*. *Mesopotamian J. Mar. Sci.* 34 (1), 27–42.

<https://doi.org/10.58629/mjms.v34i1.43>

Al-Taei, S., Abdulla, S., Lafta, A., 2014. *Longitudinal intrusion pattern of salinity in Shatt Al Arab estuary and reasons*. *J. King Abdulaziz Univ.-Mar. Sci.* 25 (2).

<https://doi.org/10.4197/Mar.25-2.10>

Baig, M., Ahmad, I., Shahfahad, Tayyab, M., Rahman, A., 2020. *Analysis of shoreline changes in Vishakhapatnam coastal tract of Andhra Pradesh, India: an application of digital shoreline analysis system (DSAS)*. *Ann. Gis.* 26 (4), 361–376.

<https://doi.org/10.1080/19475683.2020.1815839>

Ba-Khamis, A., Bilal, H., Al-Ansari, T., 2025. *Assessing Coastal Vulnerability to Sea Level Rise in Qatar: An Index-Based Approach Using Analytic Hierarchy Process*. *Climate*, 13 (11), 236.

<https://doi.org/10.3390/cli13110236>

Barillà, G., Barbaro, G., Foti, G., Mauro, G., 2025. *A New Methodology for Coastal Erosion Risk Assessment – Case Study: Calabria Region*. *J. Mar. Sci. Eng.* 13 (12), 2381.

<https://doi.org/10.3390/jmse13122381>

Chrisben Sam, S., Gurugnanam, B., 2023. *End point rate analysis and estimation along the southwest coast of Kanyakumari, Tamil Nadu, using geospatial techniques*. *Int. J. Environ. Sci. Technol.* 20 (7), 7463–7476.

<https://doi.org/10.1007/s13762-022-04374-7>

Colak, A., 2024. *Geospatial analysis of shoreline changes in the Oman coastal region (2000–2022) using GIS and remote sensing techniques*. *Front. Mar. Sci.* 11, 1305283.

<https://doi.org/10.3389/fmars.2024.1305283>

Darwish, K., Smith, S., 2023. *Landsat-Based Assessment of Morphological Changes along the Sinai Mediterranean Coast between 1990 and 2020*. *Remote Sens.-Basel.* 15 (5), 1392.

<https://doi.org/10.3390/rs15051392>

- 893 El Kafrawy, S.B., Ahmed, M.H., 2020. *Monitoring and Pro-*
 894 *tection of Egyptian Northern Lakes Using Remote Sens-*
 895 *ing Technology*. [In:] Elbeih, S., Negm, A., Kostianoy, A.
 896 (Eds.), *Environmental Remote Sensing in Egypt*. Springer,
 897 Cham, 231–284.
 898 https://doi.org/10.1007/978-3-030-39593-3_9
- 899 El-Masry, E., 2022. *Beach responses to coastal structures*
 900 *and their impacts on tourism investment, Sidi Abd El-*
 901 *Rahman coastal zone – Mediterranean Sea, Egypt*. Arab.
 902 J. Geosci. 15 (23), 1708.
 903 <https://doi.org/10.1007/s12517-022-11008-2>
- 904 Esmail, M., Mahmud, W., Fath, H., 2019. *Assessment and*
 905 *prediction of shoreline change using multi-temporal*
 906 *satellite images and statistics: Case study of Damietta*
 907 *coast, Egypt*. Appl. Ocean. Res. 82, 274–282.
 908 <https://doi.org/10.1016/j.apor.2018.11.009>
- 909 Farris, A., Long, J., Himmelstoss, E.A., 2023. *Accuracy of*
 910 *shoreline forecasting using sparse data*. Ocean. Coast.
 911 Manage. 239, 106621.
 912 <https://doi.org/10.1016/j.ocecoaman.2023.106621>
- 913 Fernández-Hernández, M., Calvo, A., Iglesias, L., Castedo, R.,
 914 Ortega, J., Diaz-Honrubia, A., Mora, P., Costamagna, E.,
 915 2023. *Anthropic Action on Historical Shoreline Changes*
 916 *and Future Estimates using GIS: Guadarmar Del Segura*
 917 *(Spain)*. Appl. Sci. 13 (17), 9792.
 918 <https://doi.org/10.3390/app13179792>
- 919 Gümüş, M., 2025. *Performance Analysis of Water Extraction*
 920 *Indices with Geospatial and Statistical Techniques Using*
 921 *Google Earth Engine Platform: A Case Study of Ramsar*
 922 *Wetlands in Türkiye*. J. Indian. Soc. Remote. Sens. 53
 923 (8), 2697–2721.
 924 <https://doi.org/10.1007/s12524-025-02180-5>
- 925 Gümüş, M., Durduran, S.S., Gümüş, K., 2022. *Investigation*
 926 *of shoreline change rates using the digital shoreline*
 927 *analysis system in Lake Beyşehir Turkey*. Bull. Geophys.
 928 Oceanograph. 63 (1), 119–142.
 929 <https://doi.org/10.4430/bgo00369>
- 930 Hashim, B., Alnaemi, A., Hussain, B., Abduljabbar, S., Doost,
 931 Z., Yaseen, Z., 2024. *Statistical downscaling of future*
 932 *temperature and precipitation projections in Iraq under*
 933 *climate change scenarios*. Phys. Chem. Earth. 135,
 934 103647. <https://doi.org/10.1016/j.pce.2024.103647>
- 935 Hashim, B., Alnaemi, A., Sultan, M., Abd Alraheem, E., Ab-
 936 duljabbar, S., Halder, B., Shahid, S., Yaseen, Z., 2025. *Im-*
 937 *pact of climate change on land use and relationship with*
 938 *land surface temperature: representative case study in*
 939 *Iraq*. Acta Geophys. 73, 3025–3043.
 940 <https://doi.org/10.1007/s11600-024-01514-0>
- 941 Himmelstoss, E., Henderson, R., Kratzmann, M., Farris, A.,
 942 2021. *Digital Shoreline Analysis System (DSAS)*. Version
 943 5.1 User Guide Open-File Report 2021-1091.
- 944 Khalifa, U., 2019. *Hydrodynamic of the Sediments Movement*
 945 *in the Southern Part of the Shatt al-Arab and North-*
 946 *Western of the Gulf*. Basrah. J. Sci. 37 (2), 237–251.
 947 <https://doi.org/10.29072/basjs.20190207>
- Lafta, A., 2021. *Influence of atmospheric forces on sea-*
 948 *surface fluctuations in Iraq marine water, northwest of*
 949 *Arabian Gulf*. Arab. J. Geosci. 14 (16), 1639.
 950 <https://doi.org/10.1007/s12517-021-07874-x>
- Lafta, A., 2023. *General characteristics of tidal currents in*
 952 *the entrance of Khor Abdullah, northwest of Arabian*
 953 *Gulf*. Oceanologia, 65 (3), 494–502.
 954 <https://doi.org/10.1016/j.oceano.2023.03.002>
- Le Cozannet, G., Bulteau, T., Castelle, B., Ranasinghe, R.,
 956 Wöppelmann, G., Rohmer, J., Bernon, N., Idier, D., Louisor,
 957 J., Salas-y-Mélie, D., 2019. *Quantifying uncertainties*
 958 *of sandy shoreline change projections as sea level rises*.
 959 Sci. Rep. 9 (1), 42.
 960 <https://doi.org/10.1038/s41598-018-37017-4>
- Long, J., Plant, N., 2012. *Extended Kalman Filter framework*
 962 *for forecasting shoreline evolution*. Geophys. Res. Lett.
 963 39 (13).
 964 <https://doi.org/10.1029/2012GL052180>
- Luijendijk, A., Hagenaars, G., Ranasinghe, R., Baart, F., Donchyts,
 966 G., Aarninkhof, S., 2018. *The State of the World's Beaches*.
 967 Sci. Rep. 8 (1), 6641.
 968 <https://doi.org/10.1038/s41598-018-24630-6>
- Mahdi, H., Mahmood, R., Muttashar, W., 2025. *Iraqi shore-*
 970 *line stability: a review of recent geological and engi-*
 971 *neering research*. Arab. J. Geosci. 18 (6).
 972 <https://doi.org/10.1007/s12517-025-12273-7>
- Mahdi, H., Muttashar, W., Mahmood, R., 2026. *Geohazards*
 974 *and coastal dynamic: a geo-engineering assessment of*
 975 *the southern Iraqi shore (Ras al-Bisha zone)*. Oceanolo-
 976 gia, 68 (1), 68107.
 977 <https://doi.org/10.5697/ZZIM7445>
- Mishra, M., Chand, P., Beja, S., Santos, C., Silva, R., Ahmed,
 979 I., Kamal, A., 2023. *Quantitative assessment of present*
 980 *and the future potential threat of coastal erosion along*
 981 *the Odisha coast using geospatial tools and statistical*
 982 *techniques*. Sci. Total Environ. 875, 162488.
 983 <https://doi.org/10.1016/j.scitotenv.2023.162488>
- Mishra, M., Bhattacharyya, D., Mondal, B., Paul, S., Silva, R.,
 985 Santos, C., Guria, R., 2025. *Forecasting shoreline dy-*
 986 *namics and land use/land cover changes in Balukhand-*
 987 *Konark Wildlife Sanctuary (India) using geospatial tech-*
 988 *niques and machine learning*. Sci. Total Environ. 975,
 989 179207.
 990 <https://doi.org/10.1016/j.scitotenv.2025.179207>
- Mishra, M., Pati, S., Paul, S., Gonçalves, R., Acharyya, T., Tri-
 992 pathy, B., Silva, R., Guria, R., Santos, C., 2024. *Dynamic*
 993 *shoreline alterations and their impacts on Olive Ridley*
 994 *Turtle (Lepidochelys olivacea) nesting sites in Gahir-*
 995 *matha Marine Wildlife Sanctuary, Odisha (India)*. Mar.
 996 Pollut. Bull. 202, 116321.
 997 <https://doi.org/10.1016/j.marpolbul.2024.116321>
- Mussa, A., Aboobacker, V., Abdulla, C., Hasna, V., Al-Ansari,
 999 E., Vethamony, P., 2024. *A climatological overview of*
 1000 *surface currents in the Arabian Gulf with special refer-*
 1001 *ence to the Exclusive Economic Zone of Qatar*. Int. J. 1002

- 1003 Climatol. 44 (13), 4677–4693.
1004 <https://doi.org/10.1002/joc.8603>
- 1005 Muttashar, W., Al-Aesawi, Q., Al-Nasrawi, A., Almayahi, D.,
1006 Jones, B., 2024. *Coastline instability evaluation: multi-*
1007 *temporal bathymetric mapping and sediment charac-*
1008 *teristics*. Environ. Earth Sci. 83 (1), 43.
1009 <https://doi.org/10.1007/s12665-023-11375-3>
- 1010 Nassar, K., Mahmud, W., Fath, H., Masria, A., Nadaoka, K.,
1011 Negm, A., 2019. *Shoreline change detection using DSAS*
1012 *technique: Case of North Sinai coast, Egypt*. Mar. Geo-
1013 *resour. Geotechnol.* 37 (1), 81–95.
1014 <https://doi.org/10.1080/1064119X.2018.1448912>
- 1015 Natesan, U., Parthasarathy, A., Vishnunath, R., Kumar, G.,
1016 Ferrer, V., 2015. *Monitoring Longterm Shoreline Changes*
1017 *along Tamil Nadu, India Using Geospatial Techniques*.
1018 *Aquat. Proc.* 4, 325–332.
1019 <https://doi.org/10.1016/j.aqpro.2015.02.044>
- 1020 Ozturk, D., Sesli, F., 2015. *Shoreline change analysis of the*
1021 *Kizilirmak Lagoon Series*. Ocean Coast. Manage. 118,
1022 290–308.
1023 <https://doi.org/10.1016/j.ocecoaman.2015.03.009>
- 1024 Palomar-Vázquez, J., Pardo-Pascual, J., Almonacid-Caballer,
1025 J., Cabezas-Rabadán, C., 2023. *Shoreline Analysis and*
1026 *Extraction Tool (SAET): A New Tool for the Automatic*
1027 *Extraction of Satellite-Derived Shorelines with Subpixel*
1028 *Accuracy*. Remote Sens. 15 (12), 3198.
1029 <https://doi.org/10.3390/rs15123198>
- 1030 Pardo-Pascual, J., Sánchez-García, E., Almonacid-Caballer, J.,
1031 Palomar-Vázquez, J., Priego de los Santos, E., Fernández-
1032 Sarría, A., Balaguer-Beser, Á., 2018. *Assessing the Accu-*
1033 *racy of Automatically Extracted Shorelines on Microti-*
1034 *dal Beaches from Landsat 7, Landsat 8 and Sentinel-2*
1035 *Imagery*. Remote Sens. 10 (2), 326.
1036 <https://doi.org/10.3390/rs10020326>
- 1037 Paul, S., Mishra, M., Guria, R., Pati, S., Baraj, B., Silva, R. da,
1038 Santos, C., 2024a. *A multi-temporal analysis of shore-*
1039 *line dynamics influenced by natural and anthropogenic*
1040 *factors: Erosion and accretion along the Digha Coast,*
1041 *West Bengal, India*. Mar. Pollut. Bull. 200, 116089.
1042 <https://doi.org/10.1016/j.marpolbul.2024.116089>
- 1043 Paul, S., Mishra, M., Pati, S., Acharyya, T., Santos, C., Silva,
1044 R. da, Guria, R., Laksono, F., 2024b. *Evaluation of over-*
1045 *wash vulnerability and shoreline dynamics in cyclone-*
1046 *prone Sagar Island, Sundarbans (India)*. Sci. Total Environ. 907,
1047 167933.
1048 <https://doi.org/10.1016/j.scitotenv.2023.167933>
- 1049 Quang, D., Ngan, V., Tam, H., Viet, N., Tinh, N., Tanaka, H.,
1050 2021. *Long-Term Shoreline Evolution Using DSAS Tech-*
1051 *nique: A Case Study of Quang Nam Province, Vietnam*. J.
1052 *Mar. Sci. Eng.* 9 (10), 1124.
1053 <https://doi.org/10.3390/jmse9101124>
- 1054 Queiroz, H., Gonçalves, R., Mishra, M., 2022. *Characterizing*
1055 *global satellite-based indicators for coastal vulnerabil-*
1056 *ity to erosion management as exemplified by a regional*
1057 *level analysis from Northeast Brazil*. Sci. Total Environ.
817, 152849. 1058
<https://doi.org/10.1016/j.scitotenv.2021.152849> 1059
- Roukounis, C., Tsihrintzis, V., 2022. *Indices of Coastal Vul-*
1060 *nerability to Climate Change: A Review*. Environ. Pro-
1061 *cess.* 9 (2), 29. 1062
<https://doi.org/10.1007/s40710-022-00577-9> 1063
- Saad, R., Gerard, J., Gerard, P., 2021. *Detection of the Shore-*
1064 *line Changes Using DSAS Technique and Remote Sens-*
1065 *ing: A Case Study of Tyre Southern Lebanon*. J. Oceanogr.
1066 *Mar. Res.* 9 (11), 1000004. 1067
- Santos, C., do Nascimento, G., Freitas, L., Batista, L., Zer-
1068 *ouali, B., Mishra, M., Silva, R., 2024. Coastal evolution*
1069 *and future projections in Conde County, Brazil: A multi-*
1070 *decadal assessment via remote sensing and sea-level*
1071 *rise scenarios*. Sci. Total Environ. 915, 169829. 1072
<https://doi.org/10.1016/j.scitotenv.2023.169829> 1073
- Santos, C., Nascimento, T. do, Mishra, M., Silva, R., 2021. *Analysis of long- and short-term shoreline change dy-*
1074 *namics: A study case of João Pessoa city in Brazil*. Sci.
1075 *Total Environ.* 769, 144889. 1076
<https://doi.org/10.1016/j.scitotenv.2020.144889> 1078
- Spinu, A., Mihailov, M., Marin, D., Cindescu, A., Nenita, R.,
1079 2025. *Assessment of Coastal Vulnerability to Hydro-Geo-*
1080 *Morphological Factors and Anthropogenic Pressures:*
1081 *A Case Study of the Romanian Black Sea Coast Using a*
1082 *Tailored Coastal Vulnerability Index*. Earth 6 (4), 158. 1083
<https://doi.org/10.3390/earth6040158> 1084
- Theocharidis, C., Doukanari, M., Kalogirou, E., Christofi, D.,
1085 Mettas, C., Kontoes, C., Hadjimitsis, D., Argyriou, A.V.,
1086 Eliades, M., 2024. *Coastal Vulnerability Index (CVI)*
1087 *Assessment: Evaluating Risks Associated with Human-*
1088 *Made Activities along the Limassol Coastline, Cyprus*.
1089 *Remote Sens.* 16 (19), 3688. 1090
<https://doi.org/10.3390/rs16193688> 1091
- Thieler, R., Hammar-Klose, E., 2000. *National Assessment*
1092 *of Coastal Vulnerability to Sea-Level Rise: Preliminary*
1093 *Results for the U.S. Pacific Coast*. 1094
- USGS, 2025. *Earth Explorer* (<https://earthexplorer.usgs.gov/>). 1095
- Vitousek, S., Buscombe, D., Vos, K., Barnard, P., Ritchie, A.,
1097 Warrick, J.A., 2023. *The future of coastal monitoring*
1098 *through satellite remote sensing*. Cambridge Prisms:
1099 *Coastal Futures*, 1, e10. 1100
<https://doi.org/10.1017/cft.2022.4> 1101
- Vos, K., Splinter, K., Harley, M., Simmons, J., Turner, I., 2019. *CoastSat: A Google Earth Engine-enabled Python toolkit*
1102 *to extract shorelines from publicly available satellite*
1103 *imagery*. Environ. Modell. Softw. 122, 104528. 1104
<https://doi.org/10.1016/j.envsoft.2019.104528> 1106
- Xu, N., 2018. *Detecting Coastline Change with All Available*
1107 *Landsat Data over 1986–2015: A Case Study for the*
1108 *State of Texas*. USA Atmos. 9 (107). 1109
<http://doi:10.3390/atmos9030107> 1110
- Yasir, M., Liu, S., Mingming, X., Wan, J., Pirasteh, S., Dang,
1111 K., 2024. *Ship Geo Net: SAR Image-Based Geometric* 1112

- 1113 *Feature Extraction of Ships Using Convolutional Neural*
1114 *Networks*. IEEE T. Geosci. Remote, 62, 1–13.
1115 <https://doi.org/10.1109/TGRS.2024.3352150>
- 1116 Zakaria, S., Al-Ansari, N., Knutsson, S., 2013. *Historical and*
1117 *Future Climatic Change Scenarios for Temperature and*
1118 *Rainfall for Iraq*. J. Civ. Eng. Archit. 7 (12).
1119 <https://doi.org/10.17265/1934-7359/2013.12.012>
- 1120 Zhang, Z., Wang, Z., Liang, B., Leng, X., Yang, B., Shi, L.,
1121 2024. *Shoreline change analysis in the estuarine area of*
1122 *Rizhao based on remote sensing images and numerical*
1123 *simulation*. Front. Mar. Sci. 11.
1124 <https://doi.org/10.3389/fmars.2024.1488577>

Impress